DIGITAL LIBRARY

dspace.vutbr.cz

Luminescent Er3+doped transparent alumina ceramics

DRDLÍKOVÁ, K.; KLEMENT, R.; DRDLÍK, D.; SPUSTA, T.; GALUSEK, D.; MACA, K.

Analog Integrated Circuits and Signal Processing
2017, vol. 37, iss. 7, pp. 2695-2703

ISSN : 0955-2219

DOI: http://dx.doi.org/10.1016/j.jeurceramsoc.2017.02.017

Accepted manuscript

© 2017. This manuscript version is made available under the CC-BY-NC-ND 4.0 license
(http://creativecommons.org/licenses/by-nc-nd/4.0/), doi: 10.1016/j.jeurceramsoc.2017.02.017
Final version available from
http://www.sciencedirect.com/science/article/pii/S0955221917300833

LUMINESCENT Er^{3+} DOPED TRANSPARENT ALUMINA CERAMICS

Katarína Drdlíková [1], Róbert Klement [2], Daniel Drdlík [1], Tomáš Spusta [1], Dušan Galusek [2], Karel Maca [1]

[1] CEITEC - Central European Institute of Technology, Brno University of Technology, Brno, Czech Republic

[2] Joint Glass Centre of the IIC SAS, TnU AD, and FChFT STU, Trenčín, Slovakia

Corresponding author: K. Drdlíková (katarina.drdlikova@ceitec.vutbr.cz)

Keywords: alumina, dopants/doping, erbium/erbium compounds, luminescence, transparent ceramics

ABSTRACT

We report on successful preparation of Er^{3+} doped transparent alumina (0.1-0.17 at. %) exhibiting visible light photoluminescence using wet shaping method and hot isostatic pressing. The effects of dopant amount, type of doping powder and powder pre-treatment on final microstructure, real in-line transmittance and photoluminescence characteristics were studied.

The real in-line transmittance ranged between 28-56 %, depending on processing parameters. The transparency decreased with increased amount of dopant. The decrease is dependent on the type of doping powder and its pre-treatment.

The photoluminescence spectra measured in both visible and NIR region showed typical emission bands due to the presence of Er^{3+} ions. The decay profiles of the $^4S_{3/2} \rightarrow {}^4I_{15/2}$ transition were fitted with a 2-exponential function, with faster component in the range of

360-700 ns and slower component around 1.6-2.4 μs. The intensity of emissions and lifetime of the $^4S_{3/2}$ level decrease significantly with increasing concentration of Er^{3+} ions.

1. INTRODUCTION

Transparent polycrystalline alumina ceramics have been studied for decades as a material for optical applications and a cheaper alternative to sapphire single crystals [1]. Besides the economic and ecological benefits of such replacement, their applications could be extended due to better mechanical properties of polycrystalline materials and possibility of production complex shaped parts.

Moreover, doping with certain elements could lead to new interesting functional properties, thus expanding the application potential of transparent aluminas even further (e.g. dosimeters, phosphors for high-brightness LEDs or laser host materials). However, adding the required amount of dopant (mostly with very low solubility in alumina lattice) inevitably leads to formation of second phase inclusions, which impair transparency, and make the preparation of transparent alumina with luminescence properties a challenging topic.

There are only few works dealing with transparent or translucent alumina doped with optically (photoluminescence - PL) active rare earth (RE) or transition metal (TM) ions. Cr-doped transparent alumina exhibiting thermoluminescence (TL) and optically stimulated luminescence was designed as a potential TL dosimetry material [2]. Doping of alumina with Ti and Mg was proposed for the same purpose [3]. However, the mean grain size of prepared material is well within the micrometer size range as the result of pressure-less sintering at relatively high temperature, with adverse impact on transparency.

Penilla et al. [4] prepared by spark plasma sintering (SPS) Tb^{3+} doped transparent alumina with fine-grained microstructure with 75 % of total transmission at a wavelength of 800 nm and with characteristic Tb^{3+} emission. According to the authors, this was the first instance

when a birefringent (non-cubic) polycrystalline oxide bulk ceramic possessed both high transparency and induced light emission properties. The authors also suggested that only high heating and cooling rates accessible by SPS technique and operating out of thermodynamic balance could result in achieving high concentration of dopant while maintaining the transparency.

Alvarez-Clemares et al. [5] showed that doping of alumina with up to 0.7 wt. % of ceria hinders the growth of alumina grains during SPS and enables the preparation of transparent alumina with total transmission of up to 70 % in the IR-VIS range. Although ceria-doped alumina exhibits photoluminescent properties [5], no measurement of the photoluminescence was performed in this work.

Sanamyan et al. [6] reported on preparation of Er - doped alumina powders (0.1 - 0.3 at. % of Er) subsequently sintered by SPS to transparent ceramics with submicron microstructure. All samples prepared under optimized conditions exhibited sharp, well-resolved emission lines characteristic for RE^{3+} ions, indicating predominantly crystalline single-site Er^{3+} occupation. Obtained IR spectra were similar to those previously observed in Er^{3+}-doped Al_2O_3 powders prepared by sol–gel technique [7]. However, the effect of Er concentration on the PL intensity was not discussed, and no data of optical transmission were provided.

Wang et al. [8] studied the influence of the phase structure and the amount of dopant on PL intensity of alumina powders. The strongest emission intensity was detected at the lowest examined concentrations (0.5 and 1 mol % Er). Dramatic concentration quenching effect took place above 1.5 mol % Er^{3+} doping concentration. At 1 mol. % Er^{3+} doping, the PL intensity of the Er^{3+}-doped Al_2O_3 powders increased with the phase structure changed in the sequence $\gamma \rightarrow \theta \rightarrow \alpha$-$(Al, Er)_2O_3$. These findings indicate that relatively low amount of Er with controllable impact on the transparency are sufficient for obtaining adequate PL intensity of doped transparent Er^{3+}-doped alumina (α-$(Al, Er)_2O_3$).

The present study follows and extends our recent work dealing with rare-earth doped transparent alumina [9], with the aim to enhance important material properties significantly (real in-line transmission, PL intensity) by modifying of the processing parameters. More precisely, it is aimed at alternative way of producing Er^{3+}-doped transparent and photoluminescent alumina, combining colloidal processing (slip casting) for green body preparation, advanced pre-sintering in a conventional electric furnace and subsequent hot isostatic pressing. Our approach differs from all cited works concerned on preparation of transparent alumina with PL properties where spark plasma sintering was applied to achieve full densification. Transparent alumina ceramics prepared in this study are characterized in terms of their microstructure (mean grain size, presence and size of secondary phase(s) inclusions), real in-line transmittance and photoluminescence properties. Contrary to all mentioned studies dealing with transparent PL alumina, the present work examines also the effect of dopant concentration and pre-treatment of doping powder on all studied characteristics.

2. EXPERIMENTAL

High purity 99.99 % commercial alumina powder (Taimicron TM-DAR, Taimei Chemicals Co., Ltd., Tokyo, Japan), with the primary particle size of 150 nm and specific surface area of 13.7 $m^2\ g^{-1}$ was used as a starting material (the values were determined by the producer from SEM micrographs and by BET analysis, respectively).

Aqueous suspensions with the solid content of 45 vol. % of Al_2O_3 were stabilized electrosterically with the use of a commercial dispersant Darvan CN. De-ionized water with room temperature electric conductivity 25 ± 5.10^{-4} S m^{-1} was used as a dispersion medium. The optically active dopant (Er) in the amount equivalent to 0.1 - 0.17 at. % of Er with respect

to Al_2O_3 was added in the form of oxide powders. Two different Er_2O_3 powders were used as starting materials.

First, a commercial coarse-grained Er_2O_3 powder (Treibacher Industrie AG, Austria) was used. In order to obtain a nano-powder, the commercial powder was dissolved in 65 % HNO_3. Citric acid dissolved in deionized water and ethylene glycol was added to the nitrate solution and heated in oil bath for 2 h at 85–90 °C. The solvent was evaporated under continuous stirring. The product was dried and calcined at 800 °C for 1h to remove organic residua. The powder was then milled in planetary mill (vessel and grinding balls from alumina) in order to reduce the number of aggregates. Residual aggregates were removed from diluted water suspension by centrifugal sedimentation at 800 rpm for 2 min. Only the particles, which remained in the suspension were dried and further used as dopants. This type of doping powder was further throughout the text denoted as P_S powder. Doped samples are denoted as P_S_x, The abbreviations are explained in Table 1.

The nano-Er_2O_3 powder (purity 99.9 %, particle size 20-30 nm, GNM – Getnanomaterials, USA) was used as received. Part of the nano-powder was also centrifugated, under the conditions described above, to remove aggregates. These types of doping powder were further throughout the text denoted as C and C_S powder, respectively. The samples doped with untreated commercial nano-powder were denoted as C_x and the samples doped with centrifuged commercial nano-powder were denoted as C_S_x.

The suspensions with added Er_2O_3 were homogenized on rollers for 24 h. 40 g of alumina milling balls with diameter 4 mm were added to 10 ml of the suspension. After homogenization, the suspensions were poured into PVC dishes and allowed to dry at ambient conditions for three days. Green bodies were then dried at 80°C for 5 h.

The samples were pre-sintered to 95–96 % of the theoretical density, which means only closed porosity was present [10, 11]. The samples doped with the P_S powder were pre-

sintered using two different regimes: single step pre-sintering (SSP) – and two-step pre-sintering (TSP) in order to establish more appropriate pre-sintering regime. Due to superior results achieved by the TSP regime only TSP was used in later experiments.

SSP was performed by heating the samples at the rate of 20 °C·min^{-1} up to the maximal temperature 1480 °C without isothermal dwell, with subsequent cooling at the same rate.

When the two-step pre-sintering (TSP) was applied, the specimens were first heated to a temperature T1 (1430-1440 °C) without isothermal dwell whereby achieving the relative density of 88 - 90 %, and subsequently cooled down to a temperature T2 (1280 °C) at the rate of 20 °C·min^{-1}. The isothermal dwell at the temperature T2 was 10 h.

The samples pre-sintered to closed porosity were hot isostatically pressed (HIP ABRA Shirp, Switzerland) at the temperature of 1280 °C for 3 h and the pressure of 200 MPa with argon used as a pressure medium. Molybdenum heating and shielding enables sintering without carbon contamination, which is usual in furnaces with graphite heating elements.

The density of sintered specimens was determined according to the Archimedes' principle. The theoretical density for all samples was calculated from the theoretical density of Al_2O_3 and Er_2O_3 by the rule of mixtures.

The microstructures were examined by scanning electron microscopy on polished and thermally etched cross sections (Lyra 3, Tescan, Czech Republic). The mean grain size was determined using the linear intercept method with a correction factor of 1.56. Minimum of 200 grains were measured in order to obtain statistically robust set of data. Distribution of Er in sintered alumina was determined using a high resolution (scanning) Transmission Electron Microscope FEI Titan Themis 60-300 (FEI, Czech Republic) equipped by Quantax EDS (Bruker Nano, Germany).

The real in-line transmission (RIT) of polished samples was measured with a non-polarized He–Ne laser (λ = 632.8 nm). The distance from the sample to the detector was 860 mm, with

an opening angle of 0.5°. The real in-line transmission was measured in at least five different positions on each sample and was recalculated to constant thickness of 0.8 mm.

The absorption spectra in the visible and NIR spectral range were recorded in the reflection mode using the Cary 5000 spectrometer equipped with the integrating sphere (module DRA-2500). The excitation and emission fluorescence spectra were measured using Fluorolog FL3-21 spectrometer (Horiba Jobin Yvon) with Xe-lamp (450 W) as an excitation source. For luminescence detection in visible and NIR spectral range, the PMT (R928) and InGaAs detector cooled with liquid nitrogen were used, respectively. The luminescence spectra of studied samples were recorded at room temperature. The luminescence decay curves were recorded at RT with the same instrument using time correlated single photon counting technique (TCSPC) with the pulsed laser diode at excitation wavelength 375 nm.

3. RESULTS

Pre-sintering regime

Green bodies of Er^{3+}-doped alumina were prepared by mixing fine alumina powder with two types of Er_2O_3 nano-powders, in some cases further pre-treated by centrifugation in order to decrease the amount of aggregates present in starting Er_2O_3 powder. The designation of individual samples is related to the preparation process and is explained in Table 1. Green bodies were pre-sintered using two different regimes: single step pre-sintering (SSP) – and two-step pre-sintering (TSP) in order to establish more appropriate pre-sintering regime. For full densification hot isostatic pressing (HIP) was performed.

Polycrystalline alumina exhibits strong dependence of optical transmittance on grain size due to its birefrigent nature [12]. Therefore, the thorough optimization of all processing parameters is needed, with special emphasis on sintering conditions. Erbium oxide was observed to retard significantly the densification of alumina: the effect was more pronounced

at higher dopant concentrations. Fig. 1 shows the comparison of sintered densities of Er^{3+}-doped samples with samples doped with negligible amount of Zr prepared in the same way in dependence on sintering temperature. The differences resulting from various amounts of the dopant were amplified at lower relative densities (RD); above 96 % of the theoretical density (TD) the sintering behavior was almost identical. This allows the use of similar sintering regimes irrespective of the amount of the dopant.

Porosity in polycrystalline alumina ceramics is usually considered to be closed if the relative density exceeds 95 % of the theoretical density [10, 11]. In order to minimize the grain size the samples pre-sintered to relative densities ranging between 95.8 and 97.8 % of TD were selected for HIP experiments. The used pre-sintering regimes and achieved relative densities are summarized in Table 2.

Based on the results from previous work [10], the temperature 1280 °C and a holding time of 3 h was selected as the most suitable conditions for hot isostatic pressing (allowing full densification without observable grain growth). All samples sintered to full density (> 99.9 % of TD); no differences could be recorded using the applied measuring method.

The values of the mean grain size (MGS) of sintered Er^{3+}-doped ceramics after HIP are summarized in the Table 3. The mean grain size of two-step pre-sintered samples seems to be slightly lower in comparison to single-step pre-sintered ones, but any difference lies within the range of the measurement error.

Microstructure of all HIP-ed samples is fine-grained and homogeneous without any second phase inclusions. Representative microstructure is shown in Fig. 2 and observable also in Fig. 3. However, some imperfections of used doping process resulted in rarely occurring aggregates of erbium oxide (Fig. 3a). This type of aggregates was found in samples doped with the P_S powder pre-sintered using single-step regime (the size of 10 – 20 μm taking into account the largest dimension). The aggregates in TSP samples were several fold smaller (3 –

10 μm) than in SSP samples (Fig. 3b). In samples doped with commercial nano-powder, SEM analysis in BSE mode (Fig. 3c) revealed only few grains with high Er content (0.3 – 0.6 μm). No larger aggregates were present. The high resolution TEM combined with EDX analysis showed enhanced concentration of Er on grain boundaries (Fig. 4), which confirmed presumed segregation of the dopant at grain boundaries. Based on SEM and TEM analyses of individual samples it can be assumed that the predominant part of the dopant is segregated at the grain boundaries. Rarely observed Er-enriched aggregates were probably the remains of aggregates present in starting powder.

Real in-line transmittance

Since the samples had thickness ranged between 0.8-1.6 mm, the measured values of RIT were recalculated to the constant thickness of 0.8 mm and are summarized in the Table 4. The RIT ranged between 28 and 56 %, and was influenced markedly by the level of Er doping. The comparison between the samples doped with the P-S powder showed that higher concentration of doping ions resulted in substantial RIT decrease. RIT was also influenced by the pre-sintering regime in case of higher dopant amount.

On the other hand, the differences between samples doped with commercial nano-powder are relatively small (Table 4) as evidenced also from macrophotographs in Fig. 5. The decrease of RIT at higher Er contents was not as sharp as in case of the powder P. However, more significant decrease of the RIT seems to be related to the way how the commercial nano-powder was pre-treated. By marginal decrease of the Er content from 0.11 at. % in the material C_0.11 to 0.1 at. % in the sample C_S_0.1 the RIT increased by 6 %, which was attributed to elimination of the aggregates by sedimentation in the material C_S_0.1.

Absorption spectra

The UV-VIS-NIR spectra of the selected samples were recorded in the reflectance mode and are depicted in Fig. 6. Characteristic absorption bands identified in the spectra correspond to intra-configurational $4f^{11}$-$4f^{11}$ electronic transitions from the Er^{3+} ground state $^4I_{15/2}$. The spectra of Er^{3+}-doped Al_2O_3 in the spectral range 300-1700 nm exhibit 12 absorptions. Particular transitions for Er^{3+} ion were labelled according to the report by Carnal et al. [13]. All the transitions are assumed to be electric dipole in nature, except for that to the $^4I_{13/2}$ first excited state that shows magnetic dipole contribution [14, 15]. The hypersensitive transitions (sensitive to variation of local structure around RE ions) in Er^{3+} ($^4I_{15/2} \rightarrow {}^2H_{11/2}$; $^4I_{15/2} \rightarrow {}^4G_{11/2}$) are clearly identified by their strong intensity. The intensity of the absorption bands increases with increasing concentration of the Er^{3+} in the host matrix. The intense band at around 240 nm, strongly overlapped with the absorbance of the Al_2O_3 matrix, can be assigned to the Er^{3+}–O^{2-} charge transfer state, although different $4f^{11} \rightarrow 4f^{10}5d$ inter-configurational transition bands of the Er^{3+} ion have also been reported in that region [16].

Photoluminescence spectra

The photoluminescence spectra of the Er^{3+}-doped Al_2O_3 at the doping level ranging between 0.1 and 0.17 at. % are shown in Fig. 7. The measured excitation spectra monitored at 548 nm (spectrum not shown) and 1529 nm were almost identical. The excitation spectra (shown in Fig. 7a) monitored at 1529 nm exhibited ten bands with barycenters at 358, 365, 379, 407, 442, 450, 487, 520, 540, and 653 nm corresponding to the excited levels $^2G_{7/2}$, $^4G_{9/2}$, $^4G_{11/2}$, $^2H_{9/2}$, $^4F_{3/2}$, $^4F_{5/2}$, $^4F_{7/2}$, $^2H_{11/2}$, $^4S_{3/2}$, and $^4F_{9/2}$, respectively. The strongest band at 379 nm corresponded to the $^4I_{15/2} \rightarrow {}^4G_{11/2}$ hypersensitive transition. The broad band, centered at 284 nm, can be assigned to the Er^{3+}–O^{2-} charge transfer state. The excitation spectra provide different possibilities of excitation to obtain green, red and near infrared (NIR) luminescence from the studied Er^{3+}-doped Al_2O_3.

The emission spectra (excited at 379 nm by Xe lamp) exhibited two green emission lines: one weaker green emission line centered at 524 nm ($^2H_{11/2}\rightarrow{}^4I_{15/2}$) and one strong emission centered at 549 nm ($^4S_{3/2}\rightarrow{}^4I_{15/2}$). Only weak red emission band corresponding to $^4F_{9/2}\rightarrow{}^4I_{15/2}$ transition was observed at about 668 nm. In the near infrared (NIR) spectral region (900-1600 nm), the emissions corresponding to $^4I_{11/2}\rightarrow{}^4I_{15/2}$ (centered at 980 nm) and $^4I_{13/2}\rightarrow{}^4I_{15/2}$ (centered at 1530 nm) transitions were observed, respectively. The broad emission band from the $^4I_{13/2}$ multiplet to the $^4I_{15/2}$ ground state is of special interest for optical amplification and laser application.

The intensity of the of green emissions in the group of samples denoted as C_S decreases with increasing concentration of Er^{3+} ions (Fig. 7b) while the intensity of the red emission only very slightly increases (i.e. no quenching of the red luminescence is observed); the relative intensity of the weak $^4F_{9/2}\rightarrow{}^4I_{15/2}$ red emission compared to green one increases. For the group of samples denoted as P_S both the green and red emission decrease with the doping concentration. The only exception is the sample C_0.11. When compared with the samples C_S_0.1 and P_S_0.1, i.e. these containing almost the same Er^{3+} doping concentration, the intensity of green emissions drops down significantly. This is most likely due to the presence of Er_2O_3 aggregates when the sedimentation step was not included during the sample preparation. The similar influence of Er^{3+} concentration on emission was observed also for emissions in NIR spectral region (Fig. 7c); the intensity of the $^4I_{13/2}\rightarrow{}^4I_{15/2}$ transition decreases, while the intensity of the $^4I_{11/2}\rightarrow{}^4I_{15/2}$ transition slightly increases with increasing Er^{3+} concentration.

Lifetime

For all samples studied the lifetime measurements have been performed in the visible spectral region for the strongest green emission centered at about 545 nm. The normalized decay

profiles of the $^4S_{3/2} \rightarrow {}^4I_{15/2}$ (green) transition are shown in Fig. 8. The decay curves were fitted with double exponential equation and the average lifetime from decay curves was calculated using the Equation 1:

$$\tau_{ave} = \frac{\int_0^\infty tIdt}{\int_0^\infty Idt} = \frac{A_1\tau_1^2 + A_2\tau_2^2}{A_1\tau_1 + A_2\tau_2} \quad (1)$$

where A_1 and A_2 are the weight factors of lifetimes τ_1 and τ_2, respectively. The corresponding lifetimes for all samples studied are summarized in Table 5.

The faster component of the decay was found to be in the range of 360-700 ns while the slower one in the range of 1.6-2.4 μs. However, in decays of the green emission the faster component dominates. The lifetime of the $^4S_{3/2}$ level decreases quite significantly with increasing concentration of Er^{3+} ions in the samples studied. The lifetime of the $^4F_{9/2}$ energy level could not be accurately measured under laser diode excitation due to the weak red emission from this level.

4. DISCUSSION

The effect of parameters of doping on final microstructure and RIT

It was demonstrated that Er inhibits densification of alumina. However, the mean grain size of all fully dense HIP-ed samples was nearly identical (~ 350 nm) with differences falling within the standard deviation of the measurement. This indicates that the optimized conditions of sintering applied in the study were appropriate in terms of minimizing the grain growth while maximizing densification during sintering.

Due to almost identical values of the mean grain size of all prepared samples, the influence of other than sintering parameters, e.g. the content and the way of pre-treatment of the Er_2O_3

powders on the RIT could be traced. Generally, with increasing Er doping the RIT decreased. However, the extent of the decrease was strongly dependent on the type of used powder and its pre-treatment (performed by centrifugal sedimentation). The highest level of RIT and the smallest decrease with increasing amount of the dopant were achieved using commercial nano-powder further treated by sedimentation and denoted as C-S (Fig. 9). Careful elimination and removal of powder aggregates, which are always present even in commercial nano-powders, could reduce the decrease of RIT observed at higher concentrations of dopant in transparent ceramics.

The nano-powder prepared by modified Pechini method and then centrifugally treated (P-S) yielded lower values of RIT than commercial nano-powder (C-S) and stronger decrease of RIT values with increasing Er concentration (Fig. 9). On the other hand, the sedimented nano-powder P prepared by modified Pechini method (P-S) yields, in terms of the RIT, results similar to those of unsedimented commercial nano-powder (C) (Fig. 9). Although not clearly documented by SEM, this indicates certain level of aggregation of doping powder, especially in case of the powder C.

The effect of pre-sintering on final microstructure and RIT

The experiments made with P-S powder showed that pre-sintering regime has some effect on the RIT values of fully dense samples after HIP. As it can be seen from Table 4, prolonged TSP regime was beneficial for increase of transparency in comparison to conventional SSP pre-sintering. Since the final grain size of the samples were not statistically different (see Table 3) and the above mentioned results indicated the importance of dopant aggregation, we concerned our attention on microstructure of sintered samples.

The aggregates present in samples pre-sintered by prolonged TSP regime (Fig. 3) were considerably smaller (3 – 10 μm) than aggregates found in sample pre-sintered without dwell

(10 – 20 μm). This confirmed the conclusions in our recently published paper [9] that long isothermal dwell (albeit at lower temperature) during two-step pre-sintering facilitates better redistribution of dopants along grain boundaries, thus decreasing the size and/or number of second phase inclusions.

Since no practical doping process allows for removal of absolutely all aggregates, the prolonged pre-sintering can be recommended for minimizing of their size.

Photoluminescence spectra

The emission spectra of the Er^{3+} doped Al_2O_3 samples both in the visible and NIR spectral range exhibit relatively broad emissions and the emission bands are inhomogeneously broadened. For some transitions, e.g. from $^4S_{3/2}$ $^4F_{9/2}$, $^4I_{11/2}$ and $^4I_{13/2}$ this indicates that the band structure is due to the Stark splitting. This effect was found to be typical for highly disordered crystalline or amorphous materials, where optical centers experience quite different local environments that result in large inhomogeneous linewidths, in some cases approaching 100 cm^{-1} or even more for 4f-4f transitions [17]. Since the optical transition frequency of an ion depends on the strain, as well as local electric and magnetic fields affecting the ion, these environmental differences lead to a distribution of these frequencies for particular type of ion; the distribution of these frequencies produce an inhomogeneously broadened line. The broadened emissions were also found for the Er^{3+}-doped Al_2O_3 thin films with relatively higher concentration of the Er^{3+} ions (2.10^{19}- 4.10^{20} cm^{-3}) in the host matrix [18]. In contrast, very well resolved and sharp structured (Stark sublevels) emissions due to the Stark or crystal field splitting were observed for lower doping levels of Er^{3+} in Al_2O_3 matrix (0.026 at. %), as reported by Sanamyan et al. [6]. Similar results were found for other Er^{3+}-doped matrixes in which the Er^{3+} ions are incorporated into the structure of the host matrix [19], and Er^{3+} ion occupies defined positions in the structure. This, together with the

fact that the emission intensity decreases with increasing concentration, point to the fact that local environment around the Er^{3+} ions is relatively disordered. The Er^{3+} ions aggregates are also possibly formed during the sample preparation that lead to the concentration quenching of luminescence due the direct interaction among Er^{3+} ions in the Al_2O_3 matrix.

Lifetime

The lifetime corresponding to $^4S_{3/2}$ level ($^4S_{3/2} \rightarrow {}^4I_{15/2}$ transition) exhibits strong dependence on the Er^{3+} concentration in Al_2O_3 host matrix (see Fig. 8, Table 5). All decay curves show non-mono-exponential profiles, even for the lowest concentrating sample containing 0.1 at. % of Er^{3+} ions ($2.38.10^{19}$ cm^{-3}), and were well fitted with double exponential decay function. It is well known that at very low concentrations of optically active ions, with negligible interactions between them, the decay of the luminescence can be described by a single exponential [20]. However, at higher concentrations the distances between active ions are shorter and the energy transfer processes become more efficient, resulting in a non-exponential decay [21]. All decay profiles thus exhibit a fast exponential decay in the initial part with a decay time of about 500 ns, followed by a slower decay with a decay time of ~ 2 μs. Similar double-exponential behavior of $^4S_{3/2}$ level decay was observed and reported by Agazzi [18] for Er^{3+}-doped Al_2O_3 films with dopant concentration in the range of 2.10^{19}-4.10^{20} cm^{-3}, with the lifetimes of 12.6 μs for faster and 30.8 μs for shorter decay process, respectively.

The observed non-exponential nature of the green luminescence decays, accompanied by shortening of the lifetimes with increasing Er^{3+} concentration is related to energy transfer processes (cross-relaxation processes) between Er^{3+} ions at higher concentrations and/or to different quenching traps (impurities and/or structural defective sites) [22]. During this process, an excited Er^{3+} ion (donor) is deactivated by transferring a part of its energy to

another neighboring Er^{3+} ion (acceptor). The energy transfer is possible if there is a certain overlap in the fluorescence emission and absorption spectra of the donor and acceptor, which is the case of concentrated Er^{3+} systems; this means that there are matching differences in acceptor and donor energy levels. Some of the possible cross-relaxation channels that depopulate thermalized $^4S_{3/2}$ level can be described as (denoted as (initial sate Er^{3+}(I), Er^{3+}(II)→final state Er^{3+}(I), Er^{3+}(II)): ($^4S_{3/2}$, $^4I_{15/2} \rightarrow {}^4I_{13/2}$, $^4I_{9/2}$), ($^4S_{3/2}$, $^4I_{15/2} \rightarrow {}^4I_{9/2}$, $^4I_{13/2}$), ($^4I_{9/2}$, $^4I_{9/2} \rightarrow {}^4I_{11/2}$, $^4F_{9/2}$), ($^4I_{9/2}$, $^4I_{11/2} \rightarrow {}^4I_{13/2}$, $^4F_{9/2}$) and other [19]. For example, in the case of ($^4S_{3/2}$, $^4I_{15/2} \rightarrow {}^4I_{9/2}$, $^4I_{13/2}$) cross-relaxation channel, the donor is deactivated without emitting green fluorescence light and as a result the intensity and lifetime are diminished. However, as mentioned above, the structural defects may also play important role in the luminescence quenching.

5. CONCLUSION

Transparent photoluminescent aluminas doped with 0.1 – 0.17 at. % Er were successfully prepared by a combination of wet shaping technique (slip casting), pressure-less pre-sintering, and hot isostatic pressing (HIP). Fully dense samples with grain size less than 400 nm exhibited the RIT values ranging between 28-56 %. The samples doped with Er_2O_3 nano-powder prepared by Pechini method exhibited slightly lower transparency (up to 52 %) due to presence of Er agglomerates in the microstructure. The RIT value of 56 % established for sample doped with commercial Er_2O_3 nano-powder is the highest real in-line transparency so far reported in the literature for luminescent RE doped aluminas. The positive influence of suspension centrifugation prior to slip casting on RIT and photoluminescence intensity was demonstrated. Upon excitation of the Er^{3+} ions in the UV range, intensive green, weak red and infrared emissions were observed, whose intensities and lifetime were described in dependence on the processing route. Based on the obtained results, future work to further

improve the optical characteristics of this type of material will be focused on optimization of dopant concentration below 0.1 at% Er.

ACKNOWLEDGEMENT

This work is part of the project 5SA14857, which has acquired the financial contribution from the EU Framework Programme for Research and Innovation Horizon 2020 within the scope of the Marie Sklodowska-Curie Actions co-financed by the South Moravian Region according to the Grant Agreement no. 665860.

The financial support of this work by the grant VEGA 1/0631/14 and GAČR 15-06390S is also gratefully acknowledged. This research has also been financially supported by the Ministry of Education, Youth and Sports of the Czech Republic under the project CEITEC 2020 (LQ1601). Part of the work was carried out with the support of core facilities of CEITEC open access project, ID number LM2011020, funded by the Ministry of Education, Youth and Sports of the Czech Republic under the activity „Projects of major infrastructures for research, development and innovations".

REFERENCES

[1] W.H. Rhodes, D.J. Sellers, T. Vasilos, Hot-Working of Aluminum-Oxide .2. Optical-Properties, J Am Ceram Soc 58(1-2) (1975) 31-34.

[2] Q. Liu, Q.H. Yang, G.G. Zhao, S.Z. Lu, H.J. Zhang, The thermoluminescence and optically stimulated luminescence properties of Cr-doped alpha alumina transparent ceramics, J Alloy Compd 579 (2013) 259-262.

[3] Q. Liu, Q.H. Yang, G.G. Zhao, S.Z. Lu, Titanium effect on the thermoluminescence and optically stimulated luminescence of Ti,Mg:alpha-Al2O3 transparent ceramics, J Alloy Compd 582 (2014) 754-758.

[4] E.H. Penilla, Y. Kodera, J.E. Garay, Blue-Green Emission in Terbium-Doped Alumina (Tb:Al2O3) Transparent Ceramics, Adv Funct Mater 23(48) (2013) 6036-6043.

[5] I. Alvarez-Clemares, G. Mata-Osoro, A. Fernandez, S. Lopez-Esteban, C. Pecharroman, R. Torrecillas, J.S. Moya, Ceria doped alumina by Spark Plasma Sintering for optical applications, J Eur Ceram Soc 32(11) (2012) 2917-2924.

[6] T. Sanamyan, R. Pavlacka, G. Gilde, M. Dubinskii, Spectroscopic properties of Er3+-doped alpha-Al2O3, Opt Mater 35(5) (2013) 821-826.

[7] A.A. Kaplyanskii, A.B. Kulinkin, A.B. Kutsenko, S.P. Feofilov, R.I. Zakharchenya, T.N. Vasilevskaya, Optical spectra of triply-charged rare-earth ions in polycrystalline corundum, Phys Solid State+ 40(8) (1998) 1310-1316.

[8] X.J. Wang, M.K. Lei, T. Yang, H. Wang, Phase structure and photoluminescence Al2O3 powders prepared by the properties of Er3+-doped sol-gel method, Opt Mater 26(3) (2004) 247-252.

[9] K. Bodišová, R. Klement, D. Galusek, V. Pouchlý, D. Drdlík, K. Maca, Luminescent rare-earth-doped transparent alumina ceramics, J Eur Ceram Soc 36(12) (2016) 2975-2980.

[10] M. Trunec, K. Maca, R. Chmelik, Polycrystalline alumina ceramics doped with nanoparticles for increased transparency, J Eur Ceram Soc 35(3) (2015) 1001-1009.

[11] T. Spusta, J. Svoboda, K. Maca, Study of pore closure during pressure-less sintering of advanced oxide ceramics, Acta Mater 115 (2016) 347-353.

[12] R. Apetz, M.P.B. van Bruggen, Transparent alumina: A light-scattering model, J Am Ceram Soc 86(3) (2003) 480-486.

[13] W.T. Carnall, H. Crosswhite, H.M. Crosswhite, Energy level structure and transitions probabilities of the trivalent lanthanides in LaF3 Argonne National Laboratory, Special Report1977.

[14] M.J. Weber, Probabilities for Radiative and Nonradiative Decay of Er3+ in Laf3, Phys Rev 157(2) (1967) 262-&.

[15] C.M. Dodson, R. Zia, Magnetic dipole and electric quadrupole transitions in the trivalent lanthanide series: Calculated emission rates and oscillator strengths, Phys Rev B 86(12) (2012).

[16] P. Dorenbos, The 4f(n)<-> 4f(n-1)5d transitions of the trivalent lanthanides in halogenides and chalcogenides, J Lumin 91(1-2) (2000) 91-106.

[17] G. Liu, B. Jacquier, Spectroscopic Properties of Rare Earths in Optical Materials, Springer Berlin Heidelberg2006.

[18] L. Agazzi, Spectroscopic Excitation and Quenching Processes in Rare-Earth-Ion-Doped Al2O3 and their Impact on Amplifier and Laser Performance, University of Twente, The Netherlands, 2012.

[19] V. Venkatramu, S.F. Leon-Luis, U.R. Rodriguez-Mendoza, V. Monteseguro, F.J. Manjon, A.D. Lozano-Gorrin, R. Valiente, D. Navarro-Urrios, C.K. Jayasankar, A. Munoz, V. Lavin, Synthesis, structure and luminescence of Er3+-doped Y3Ga5O12 nano-garnets, J Mater Chem 22(27) (2012) 13788-13799.

[20] P. Babu, H.J. Seo, C.R. Kesavulu, Y.H. Jang, C.K. Jayasankar, Thermal and optical properties of Er3+-doped oxyfluorotellurite glasses, J Lumin 129(5) (2009) 444-448.

[21] B. Dibartolo, Energy Transfer Processes in Condensed Matter, Springer US1984.

[22] V. Venkatramu, M. Giarola, G. Mariotto, S. Enzo, S. Polizzi, C.K. Jayasankar, F. Piccinelli, M. Bettinelli, A. Speghini, Nanocrystalline lanthanide-doped Lu3Ga5O12 garnets: interesting materials for light-emitting devices, Nanotechnology 21(17) (2010).

Figure captions

Fig. 1. Dependence of relative density of Er^{3+}-doped alumina on the sintering temperature (pressure-less sintering). For comparison, the densification data of alumina doped with 250 ppm Zr are also present.

Fig. 2. The representative microstructure of HIPed alumina doped by Er.

Fig. 3. The Er-enriched aggregates and grains found in the HIPed samples doped using:

a) P_S powder pre-sintered by single step pre-sintering

b) P_S powder pre-sintered by two-step pre-sintering

c) C_S powder pre-sintered by two-step pre-sintering

Fig. 4. TEM image of Er^{3+}-doped alumina (0.1 at. % of Er^{3+}) microstructure and EDS mapping for Al, O and Er elements on the grain boundary.

Fig. 5. Transparent Er^{3+}-doped alumina. The samples are ca 3 cm in diameter and they are positioned 1 cm above the text.

Fig. 6. Diffuse reflectance spectra of the Al_2O_3:Er^{3+} ceramics in the UV-VIS-NIR range recorded at RT (a). The expanded segment of the spectra with corresponding absorption bands assignment (b). All transitions start from $^4I_{15/2}$ ground state to the indicated levels.

Fig. 7. Luminescence spectra of the Al_2O_3:Er^{3+} doped ceramics: (a) The representative excitation spectrum monitored at 1529 nm with corresponding band assignment; Emission

spectra of the Er^{3+} doped Al_2O_3 ceramics monitored in VIS (b) and NIR (c) spectral region after sample excitation at 379 nm.

Fig. 8. Er^{3+} luminescence decay curves of the green emission ($^2H_{11/2}$, $^4S_{3/2} \rightarrow {}^4I_{15/2}$) recorded at RT under laser diode excitation at 375nm: (a) The decay curves were fitted with 2-exponential decay function. (b) The dependence of τ_{ave} on Er^{3+} concentration.

Fig. 9. The real in-line transmittance – Er content dependence.

Table captions

Table 1. Abbreviation in designation of samples

Table 2. Pre-sintering regimes for individual samples and achieved relative densities

Table 3. Mean grain size of rare earth doped alumina after HIP (1280°C / 3 h, 200 MPa)

Table 4. Real in-line transmittance of rare earth doped alumina after HIP (1280°C / 3 h, 200 MPa)

Table 5. Lifetimes of the $^4S_{3/2}$ level at RT obtained under excitation at 375 nm

Table 1

Abbreviation in designation of samples	Meaning in relation to the preparation of samples
P	Nano-powder prepared by modified Pechini method
C	Commercial nano-powder
S	Sedimentation used for removal of the aggregates
x	at. % of Er with respect to Al_2O_3

Table 2

Sample	SSP – regime [a)]	SSP – RD [%]	TSP – regime [a)]	TSP – RD [%]
P_S_0.1	1480 °C	97.2	1430 °C → 1280 °C / 10 h	96.9
P_S_0.17	1480 °C	96.4	1440 °C → 1280 °C / 10 h	95.8
C_S_0.1	-	-	1440 °C → 1280 °C / 10 h	97.4
C_S_0.125	-	-	1440 °C → 1280 °C / 10 h	96.9
C_S_0.15	-	-	1440 °C → 1280 °C / 10 h	96.2
C_ 0.11	-	-	1440 °C → 1280 °C / 10 h	97.8

[a)] SSP – without dwell; TSP – without dwell in the first step

Table 3

Sample	SSP + HIP		TSP + HIP	
	MGS [nm]	SD[a)]/n[b)] [nm/-]	MGS [nm]	SD[a)]/n[b)] [nm/-]
P_S_0.1	450	60 / 20	390	50 / 20
P_S_0.17	370	50 / 20	350	40 / 20
C_S_0.1	-	-	350	40 / 20
C_S_0.125	-	-	330	30 / 20
C_S_0.15	-	-	350	30 / 20
C_ 0.11	-	-	340	40 / 20

[a)] SD is the standard deviation; [b)] n is the number of measurements

Table 4

Sample	RIT after SSP + HIP [%]	RIT after TSP + HIP [%]
P_S_0.1	49	52
P_S_0.17	28	34
C_S_0.1	-	56
C_S_0.125	-	53
C_S_0.15	-	53
C_ 0.11	-	50

Table 5

Sample	Er^{3+}concentration [at.%]	τ_1[a)] [ns]	τ_2[a)] [μs]	τ_{ave} [μs]
C_S_0.1	0.1	694 (76%)	2.43 (24%)	1.61
C_0.11	0.11	566 (81%)	2.20 (19%)	1.34
C_S_0.125	0.125	545 (86%)	2.04 (14%)	1.11
C_S_0.15	0.15	517 (84%)	1.74 (16%)	0.99
P_S_0.1	0.1	564 (85%)	2.00 (15%)	1.12
P_S_0.17	0.17	360 (91%)	1.64 (9%)	0.75

[a)] The numbers in parenthesis represent the weight of particular lifetime in the average lifetime value.

Fig 1

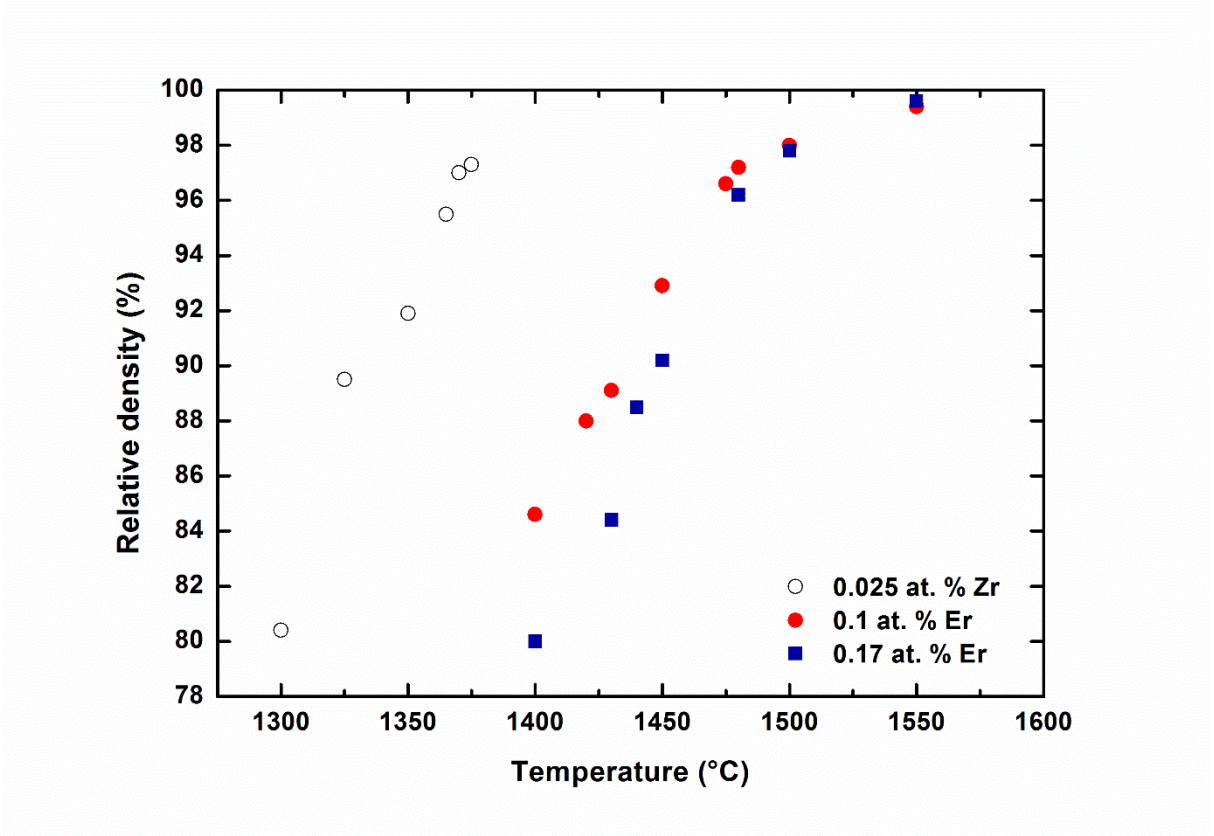
Relative density (%)
Temperature (°C)
100
98
96
94
92
90
88
86
84
82
80
78
1300
1350
1400
1450
1500
1550
1600
0.025 at. % Zr
0.1 at. % Er
0.17 at. % Er

Fig. 2

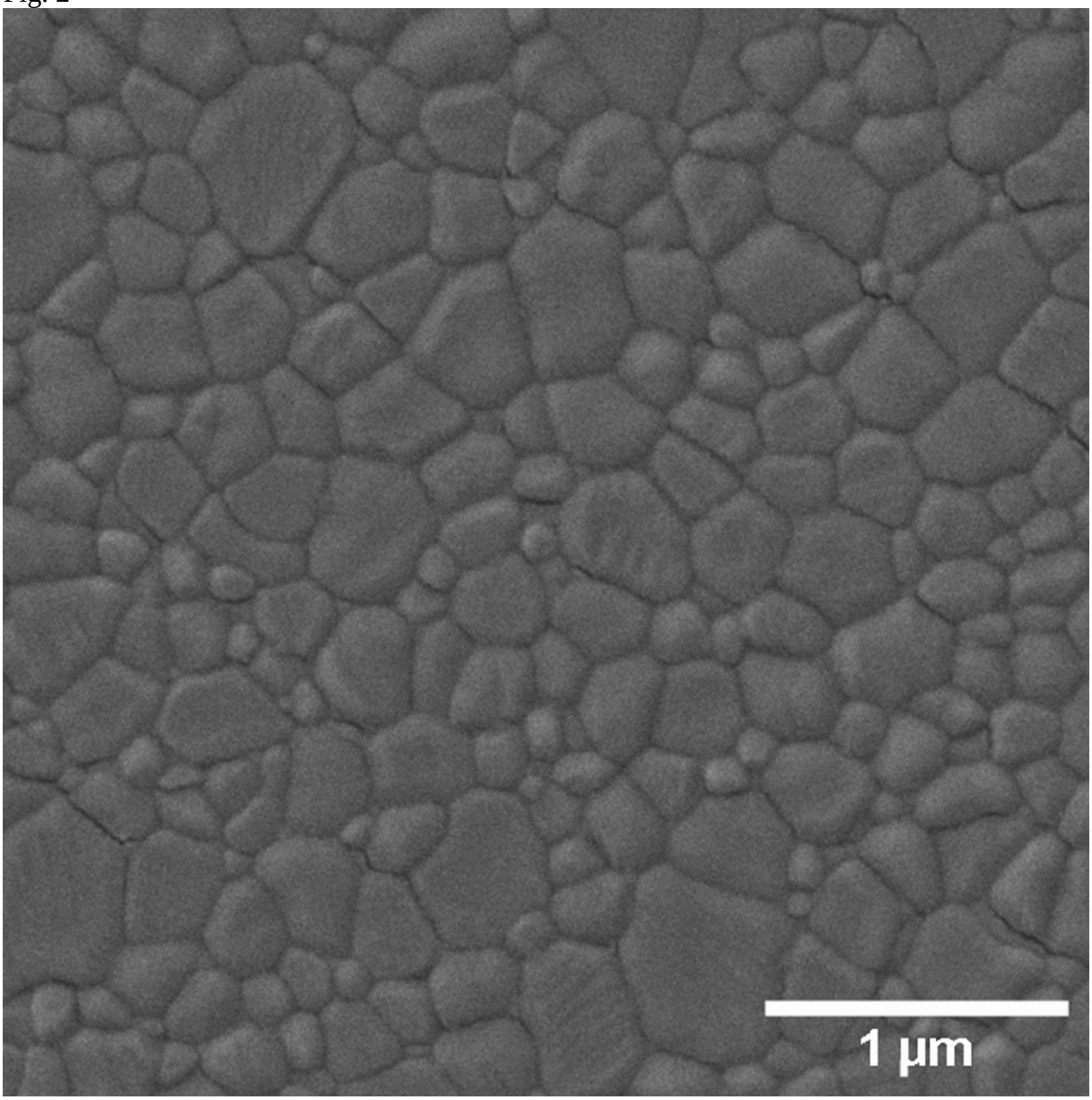

Fig. 3

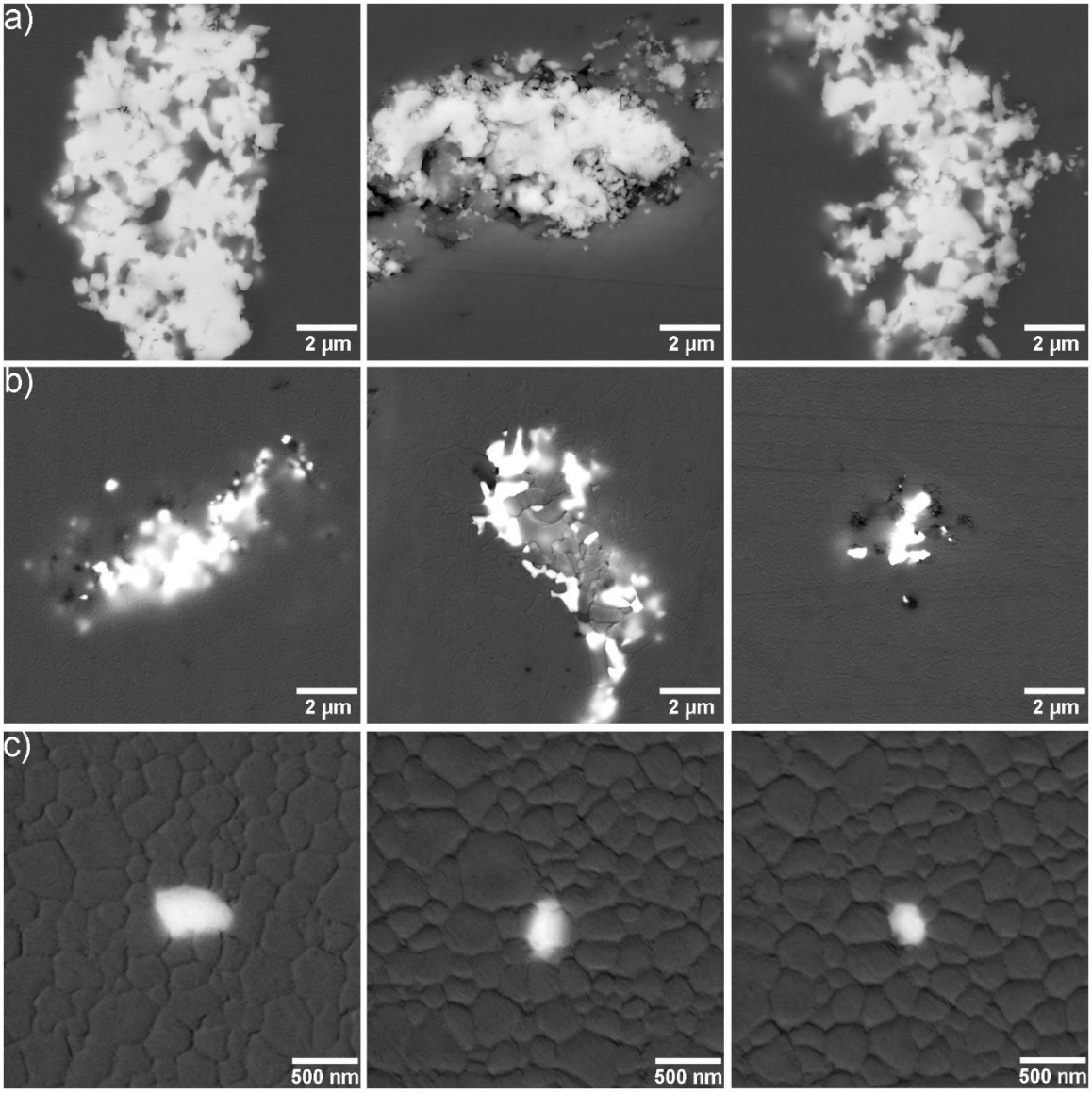

Fig. 4

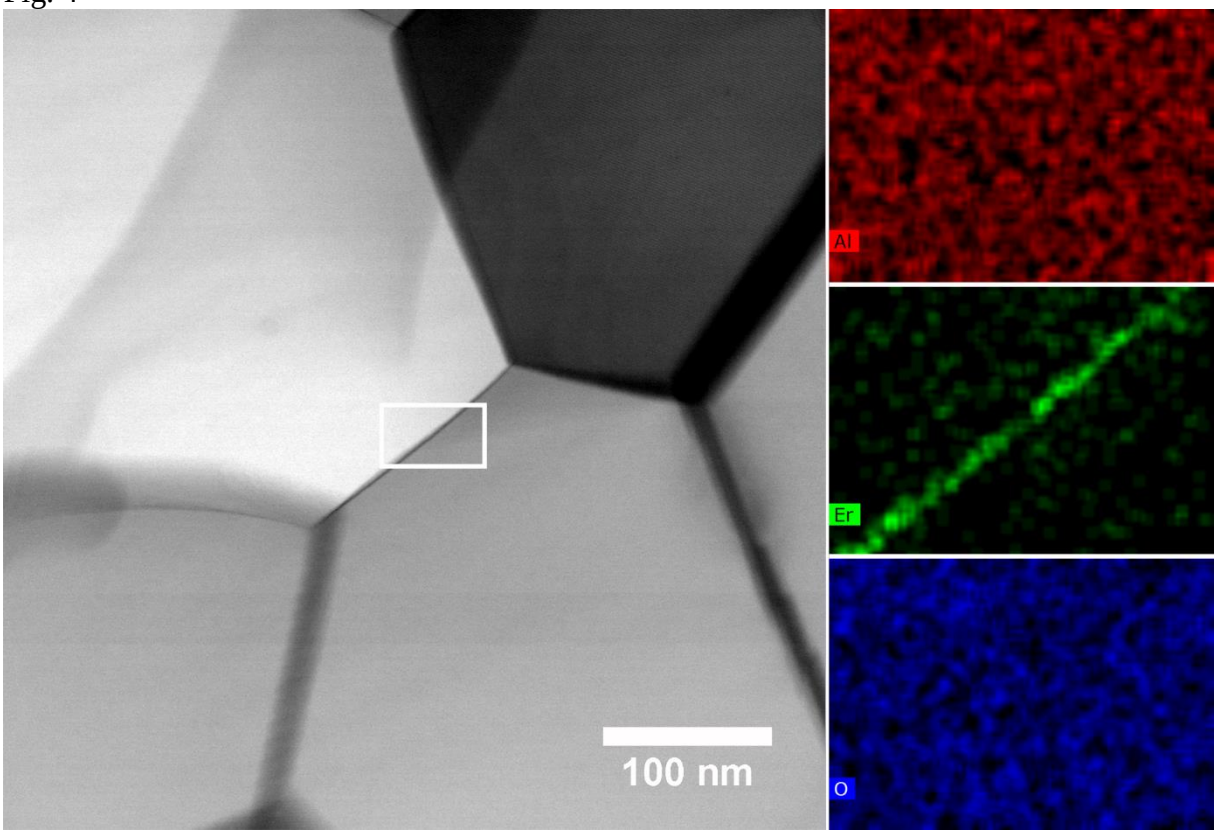

Fig. 5

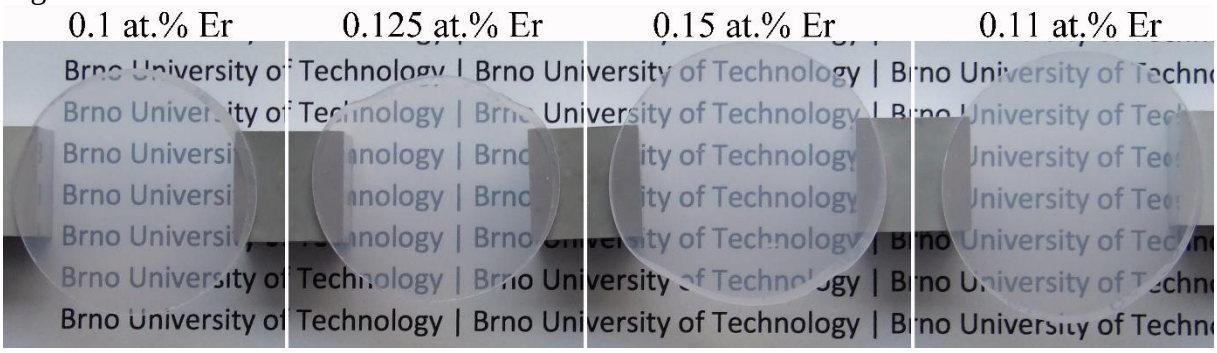

Fig. 6a

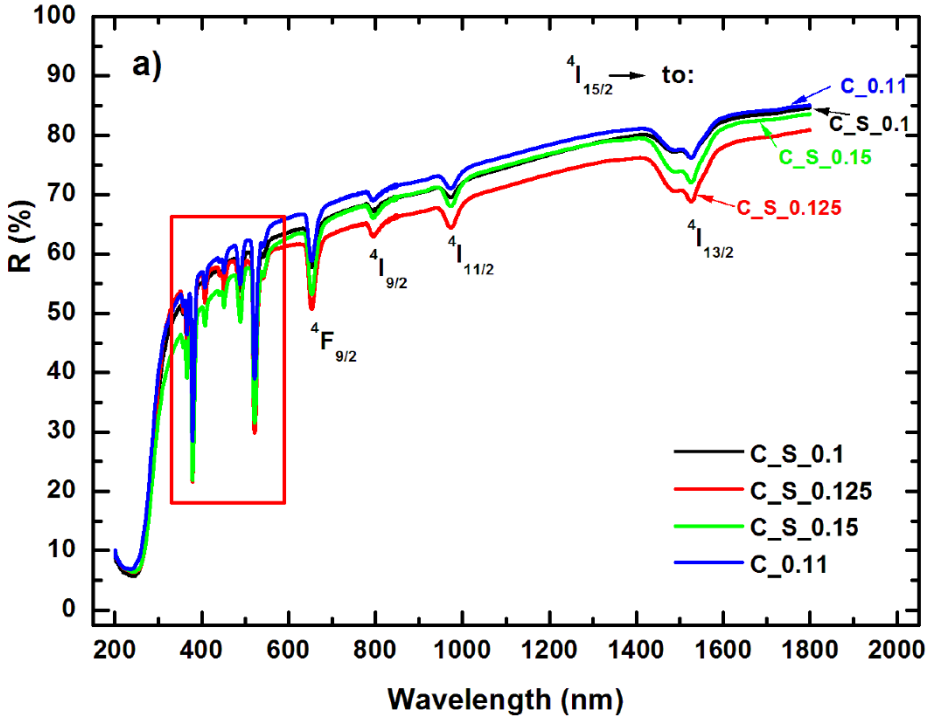
a)
$^4I_{15/2}$ → to:
C_0.11
C_S_0.1
C_S_0.15
C_S_0.125
$^4I_{13/2}$
$^4I_{9/2}$
$^4I_{11/2}$
$^4F_{9/2}$
C_S_0.1
C_S_0.125
C_S_0.15
C_0.11
R (%)
Wavelength (nm)
0
10
20
30
40
50
60
70
80
90
100
200
400
600
800
1000
1200
1400
1600
1800
2000

Fig. 6b

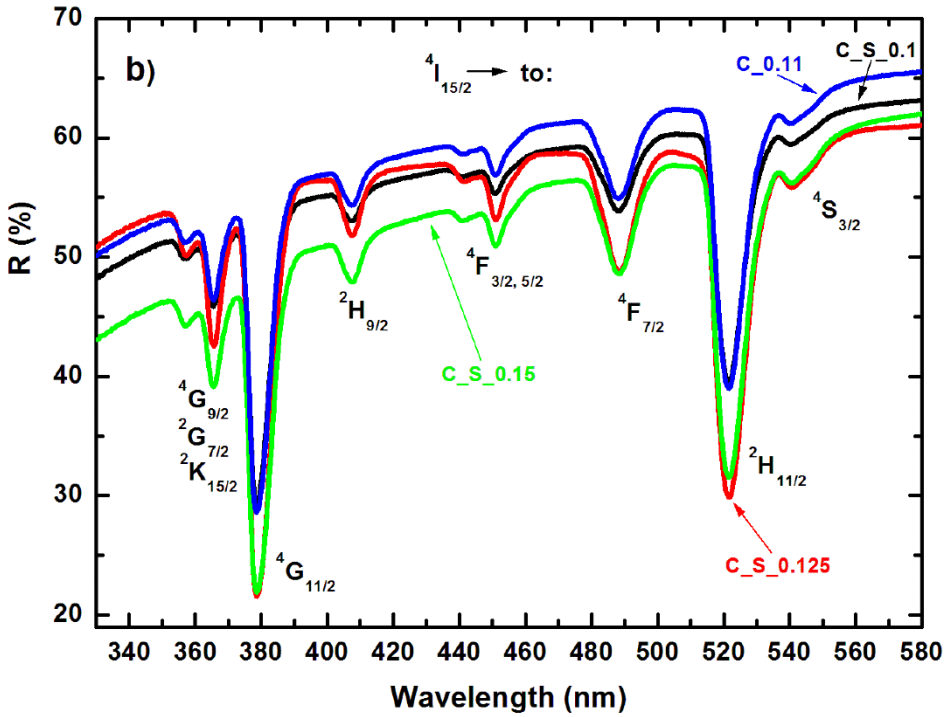
b)
$^4I_{15/2}$ → to:
C_0.11
C_S_0.1
C_S_0.15
C_S_0.125
$^4G_{9/2}$
$^2G_{7/2}$
$^2K_{15/2}$
$^4G_{11/2}$
$^2H_{9/2}$
$^4F_{3/2, 5/2}$
$^4F_{7/2}$
$^2H_{11/2}$
$^4S_{3/2}$
R (%)
Wavelength (nm)
70
60
50
40
30
20
340
360
380
400
420
440
460
480
500
520
540
560
580

Fig. 7a

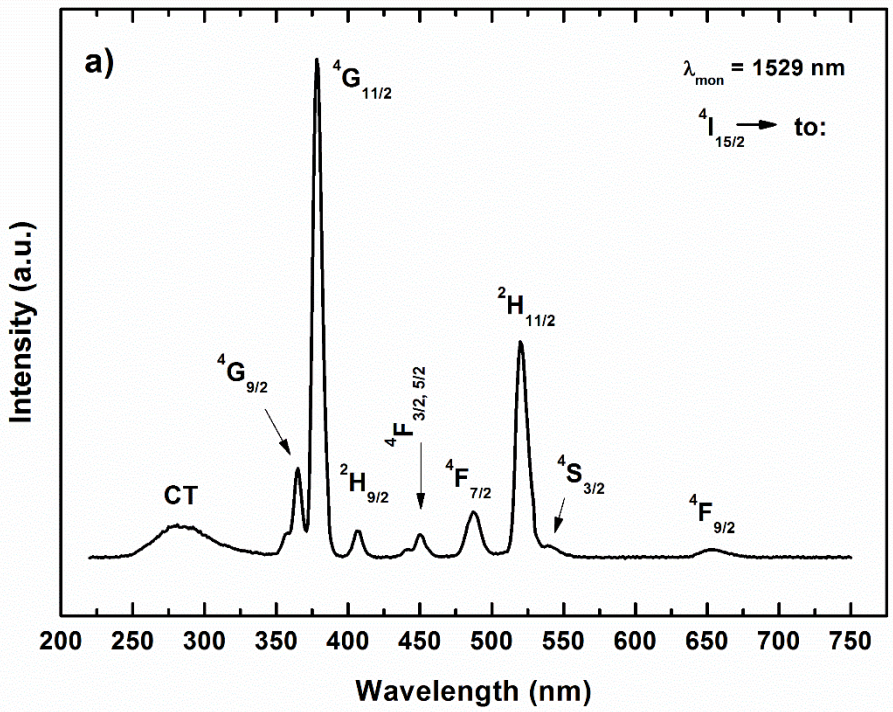
a)
λ_{mon} = 1529 nm
$^4I_{15/2}$ → to:
$^4G_{11/2}$
$^2H_{11/2}$
$^4G_{9/2}$
$^4F_{3/2, 5/2}$
$^2H_{9/2}$
$^4F_{7/2}$
$^4S_{3/2}$
$^4F_{9/2}$
CT
Intensity (a.u.)
200 250 300 350 400 450 500 550 600 650 700 750
Wavelength (nm)

Fig. 7b

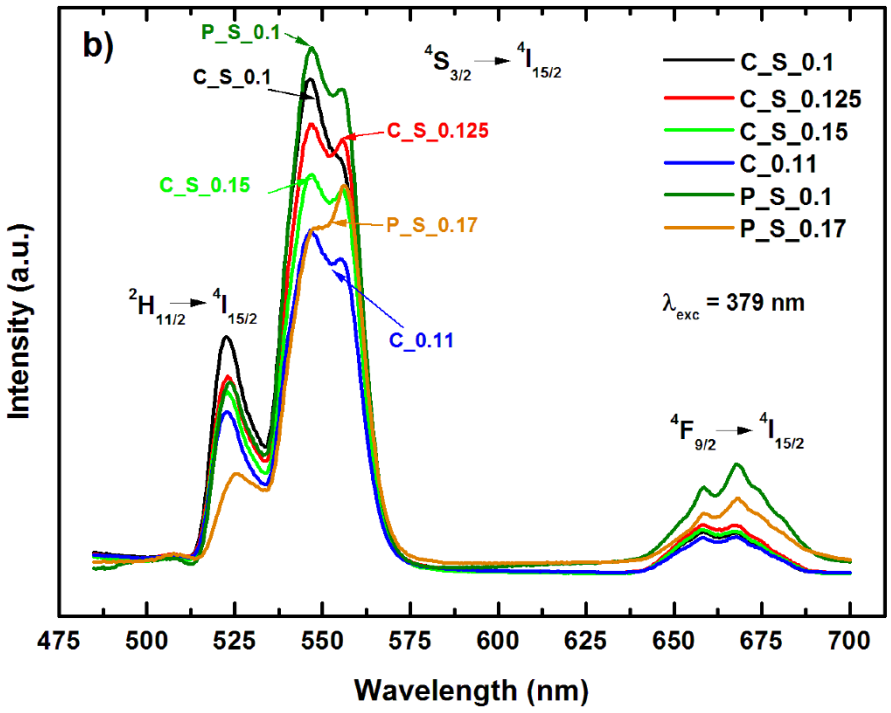
b)
P_S_0.1
C_S_0.1
C_S_0.125
C_S_0.15
P_S_0.17
C_0.11
$^4S_{3/2} \rightarrow {}^4I_{15/2}$
$^2H_{11/2} \rightarrow {}^4I_{15/2}$
$^4F_{9/2} \rightarrow {}^4I_{15/2}$
λ_{exc} = 379 nm
C_S_0.1
C_S_0.125
C_S_0.15
C_0.11
P_S_0.1
P_S_0.17
Intensity (a.u.)
475
500
525
550
575
600
625
650
675
700
Wavelength (nm)

Fig. 7c

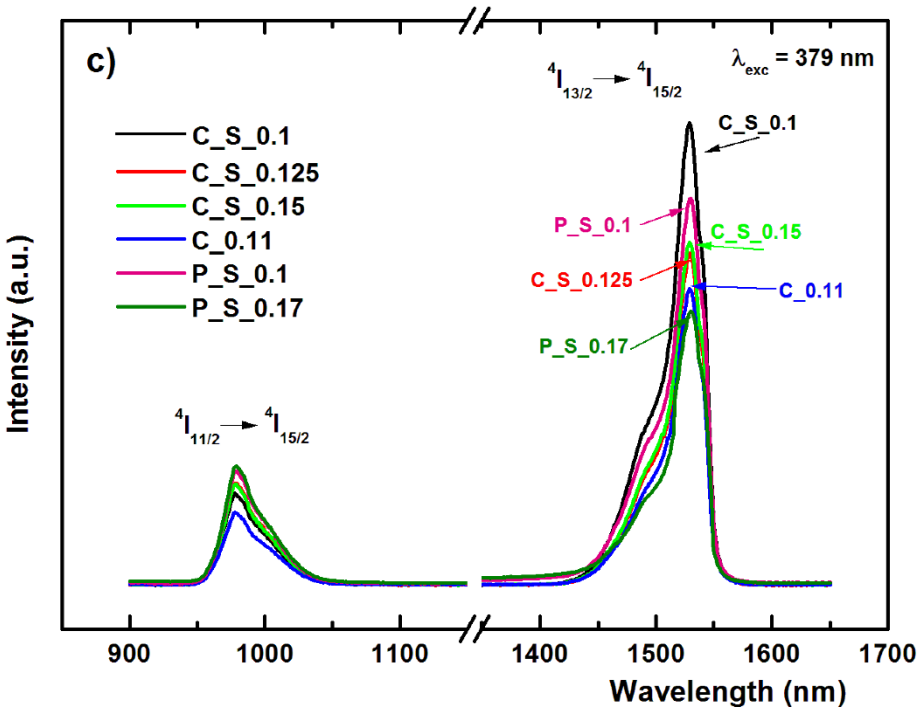
c)
λexc = 379 nm
4I13/2 → 4I15/2
4I11/2 → 4I15/2
C_S_0.1
C_S_0.125
C_S_0.15
C_0.11
P_S_0.1
P_S_0.17
Intensity (a.u.)
Wavelength (nm)
900
1000
1100
1400
1500
1600
1700

Fig. 8a

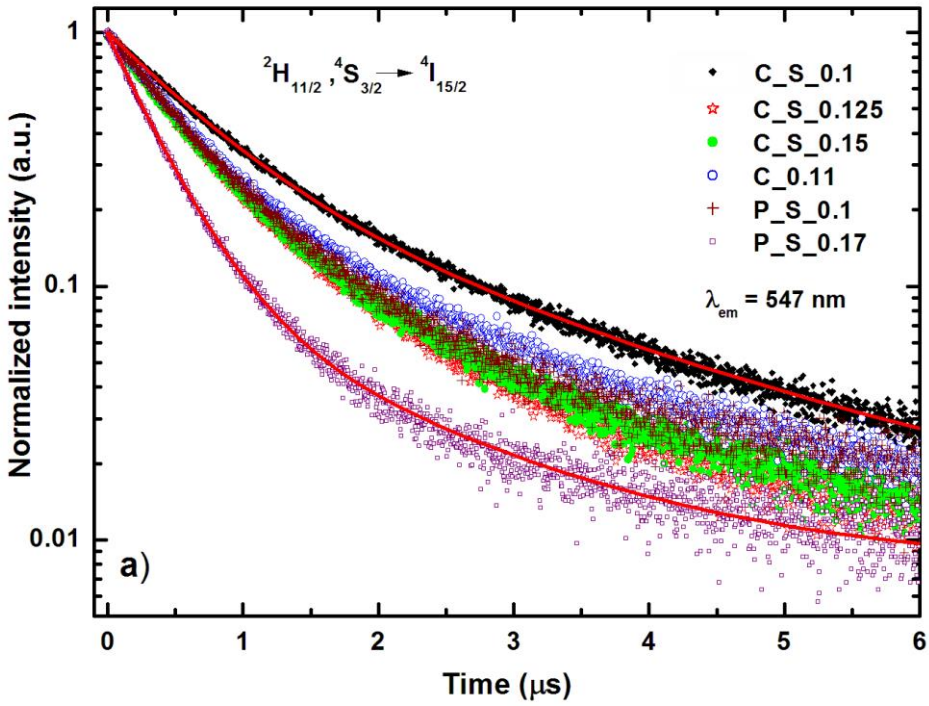
Normalized intensity (a.u.)
1
0.1
0.01
0
1
2
3
4
5
6
Time (μs)
a)
$^2H_{11/2}, ^4S_{3/2} \rightarrow ^4I_{15/2}$
C_S_0.1
C_S_0.125
C_S_0.15
C_0.11
P_S_0.1
P_S_0.17
λ_{em} = 547 nm

Fig. 8b

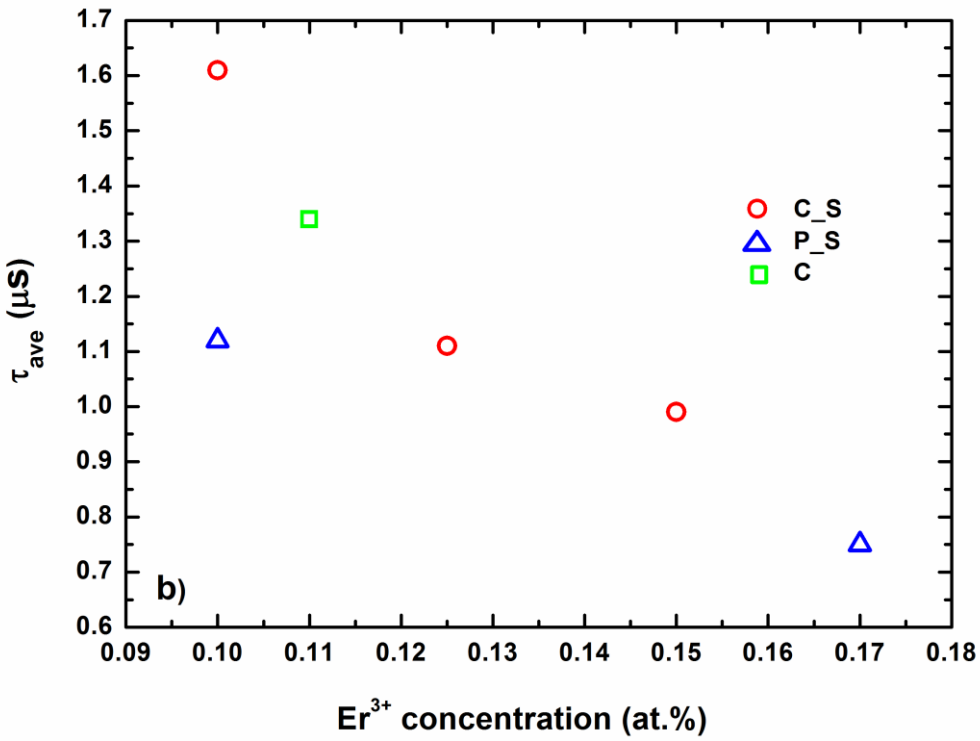
1.7
1.6
1.5
1.4
1.3
1.2
1.1
1.0
0.9
0.8
0.7
0.6
τave (μS)
b)
C_S
P_S
C
0.09
0.10
0.11
0.12
0.13
0.14
0.15
0.16
0.17
0.18
Er3+ concentration (at.%)

Fig. 9

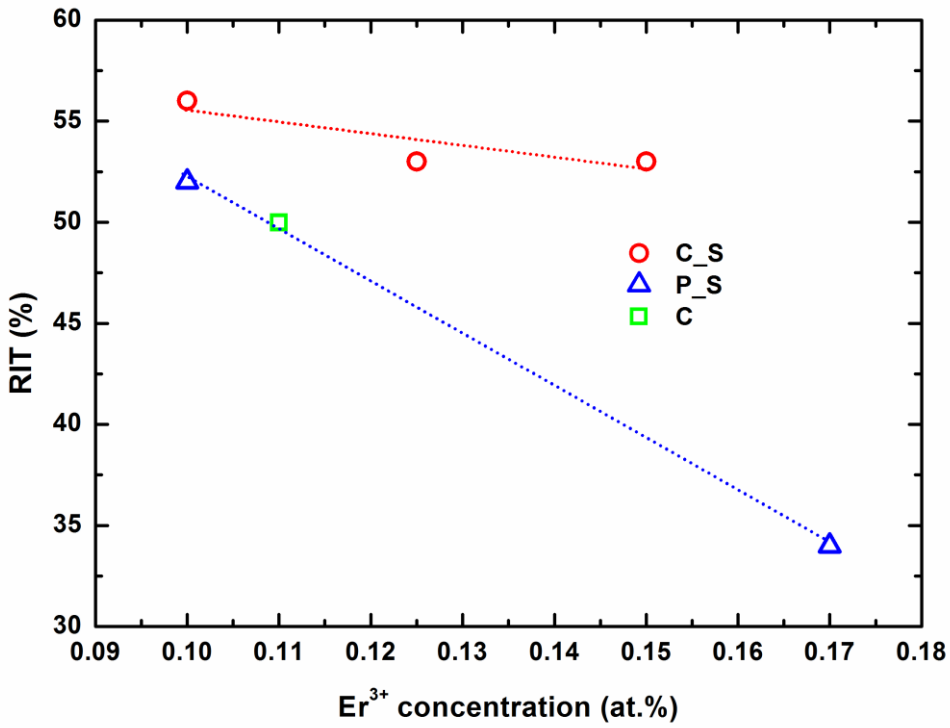
60
55
50
45
40
35
30
RIT (%)
0.09
0.10
0.11
0.12
0.13
0.14
0.15
0.16
0.17
0.18
Er3+ concentration (at.%)
C_S
P_S
C